Reporting the Behavior and Reliability of Inductor in a 12 V to 24 V Transformerless DC-DC Boost Converter: A Design-Oriented Analysis

Kuldeep Jayaswal*‡, D. K. Palwalia*, Josep M. Guerrero**

*Department of Electrical Engineering, Rajasthan Technical University, Kota, 324010, India

**Centre for Research on Microgrid (CROM), AAU Energy, Aalborg University, 9220, Aalborg, Denmark

(Kuldeep12555@gmail.com, dkpalwalia@rtu.ac.in, joz@et.aau.dk)

‡Corresponding Author; Kuldeep Jayaswal, Rajasthan Technical University, Kota, 324010, India,

Tel: +918949639383, Kuldeep12555@gmail.com

Received: 30.10.2023 Accepted:19.12.2023

Abstract- In the modern era of power electronics, transformerless DC-DC boost converters have gained prominence owing to their simplicity, reduced size, and enhanced efficiency in renewable energy applications. In DC-DC boost converters, the optimal design of an inductor, also known as the 'Heart' of the converter, is essential for facilitating energy transfer and optimizing conversion efficiency. In this paper, the behavior and reliability of an inductor have been analyzed and reported through its design & comprehensive performance investigation within a 12 V to 24 V transformerless DC-DC boost converter. The '*Area Product Method (APM)*' has been utilized to design the inductor through analyzing the factors likewise magnetic length, area of its window, significant turns count, cross-section area, and size of wire. Observations have been made by examining the inductor's performance in relation to output current and load resistance at frequencies of 100 kHz and 500 kHz. In addition, a power loss assessment has also been conducted to analyze the behavior and assess its impact on reliability by comparing it to other power components. This analysis highlights the inductor's performance at different operating conditions. Further, this paper extends its focus toward evaluating the reliability and instances of failure aspects of the inductor by comparing it with other power components in the DC-DC boost converter. The findings clearly demonstrate the inductor's superior reliability, exhibiting a notably lower failure rate in comparison to other power components. It confirms the durability and sustained performance of inductor. MATLAB® Simulink platform has been used for analyzing the results.

Keywords Transformerless DC-DC boost converter, design of inductor, renewable energy application, reliability analysis.

1. Introduction

The increasing demand for effective and versatile energy conversion within the evolving area of power electronics has driven notable progress in converter technologies. DC-DC converters are essential for facilitating voltage conversion across a wide range of uses, including compact electronic systems, renewable energy platforms, and electric vehicles. These converters are essential for ensuring the appropriate voltage levels required by different systems [1]. A typical power electronic converter system consists of two main stages, illustrated in Fig. 1. In the 'Power stage,' the converter processes the electrical signal, that can be either AC or DC, depending on the specific application requirements [2], [3]. This stage often incorporates critical components such as diodes, switches, and filters to regulate incoming power effectively [4], [5]. On the other hand, the 'Control stage' is responsible for managing the overall operation of the converter. It includes controllers, sensors, and feedback mechanisms that monitor the system's performance and make necessary adjustments to optimize converter functionality [6].

Figure 2 demonstrates the physical design of inductor within transformerless DC-DC converter topologies like Buck, Boost, and Buck-Boost converters. The inductor, a passive electronic component, stores energy in the form of a magnetic field [7-10]. It comprises a wound wire coil which

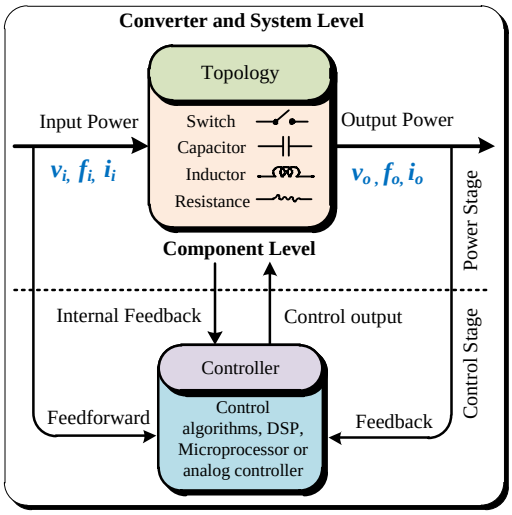


Fig. 1. The design of an electronic converter system.

encircling a central core, typically made of ferromagnetic material [11-13]. The core enhances the efficiency of magnetic energy storage.

The inductor is referred to as the central component of the conversion mechanism. Designing process of the inductor has posed considerable challenges for researchers for a long time, consequently influencing the overall system operation and its performance. Several reports have focused on calculating the inductor value rather than adhering to proper design criteria and an evaluation process, areas that still require careful consideration [11], [12], [15].To attain the required minimum inductance for the desired output, accurate information regarding the number of turns, core type, core size, air gap measurement, and related aspects are crucial [16, 17], [33]. The selection of core type, size, and proper air gap measurement plays a pivotal role in the design and performance of electromagnetic components, particularly in inductors [24]. Various core types, such as toroidal, E-core, and U-core, offer distinct advantages based on application requirements [25]. The choice between them involves trade-offs in factors like magnetic flux, efficiency, and size. Toroidal cores, for instance, provide uniform magnetic fields and efficient energy transfer due to their closed-loop structure [14]. The absence of air gaps in toroidal cores minimizes magnetic flux leakage, contributing to enhanced performance and reduced electromagnetic interference.

However, manufacturing complexities and cost considerations may influence the selection of alternative core types [26], [14]. Core size, denoted by factors like cross-sectional area and volume, directly impacts the overall size and weight of the electromagnetic [27], [32]. Smaller cores are generally preferred for applications with stringent space constraints, while larger cores may be chosen for applications prioritizing efficiency and power handling. Air gap measurement is a critical aspect, especially in inductors, as it affects magnetic reluctance and thus the overall magnetic circuit [25], [24]. Accurate control of the air gap is crucial for achieving desired magnetic characteristics, and variations in gap dimensions can significantly impact performance. Advanced measurement techniques, such as non-contact methods and automated systems, have been used to ensure accuracy in air gap control [14], [28-31].

In the area of electronics engineering, the concept of reliability stands as a paramount factor in ensuring the consistent and predictable performance of components, devices, and systems [18]. Reliability evaluation, accompanied by failure rate analysis, emerges as a vital process to gauge the operational dependability of inductor in these intricate systems [19-22]. The calculation of the failure rate for each component robust designs and helps in the selection of components offers valuable insights into the failure behavior of the individual parts. It also contributes to the development of that align with the desired reliability standards [17-21].

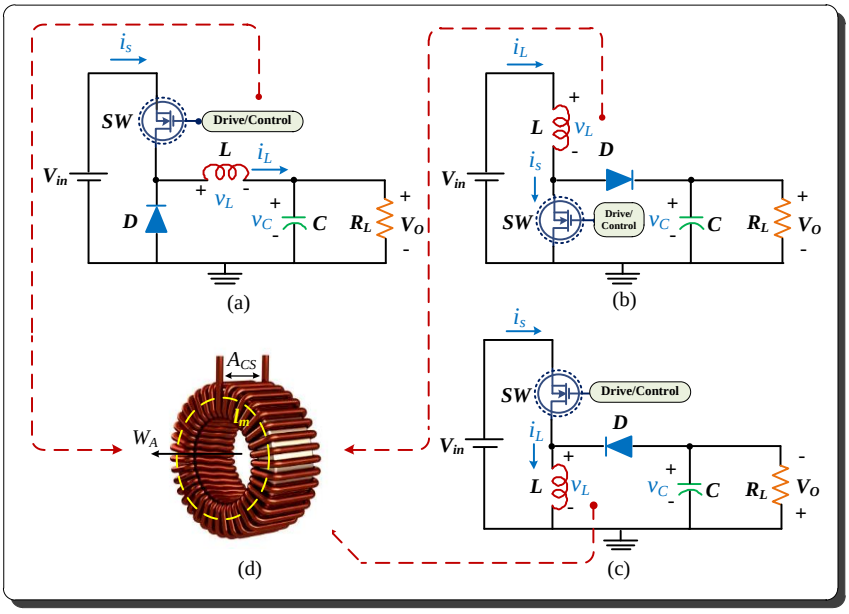


Fig. 2. Transformerless DC-DC converter topologies (a) Buck configuration (b) Boost configuration (c) Buck-Boost configuration (d) design of inductor (toroid).

This research paper mainly focuses on the design & reliability analysis of the inductor at 100kHz frequency. In the inductor design process, the 'Area Product Method (APM)' has been utilized to assess critical parameters, including the window area (W_A), magnetic length (l_m), cross-sectional area (A_{CS}), turn counts (N), and wire gauge (SWG: Standard Wire Gauge) [14-17]. Additionally, a detailed performance analysis of the inductor has been conducted, taking into consideration factors such as output current at operating frequencies of 100 kHz and 500 kHz. The behavior and the performance of the inductor have also been investigated through power loss analysis. Various novel reportings have been made by investigating these losses for each power component like switch, diode, inductor, and capacitor. Special emphasis has been directed towards evaluating the reliability of the inductor, involving a thorough examination of its failure rate. The comparative performance evaluation has been broadened to examine the failure rate and reliability of other power elements like MOSFET, D, C, and R_L. These evaluations provide valuable insights into the predicted operating lifespan and possible patterns of failures of each component.

The paper is organized in a logical flow: Section 1 introduces the topic and establishes the context through a rigorous literature survey, Sections 2 and 3 provide the physical significance of the inductor and the converter's operation for understanding its role through establishing some formula for calculating the value of duty cycle, inductor, capacitance, and ripple current, Sections 4 provides the inductor design process through area product method to evaluate the essential factors such as area of window (W_A) & its cross-section (A_{CS}), magnetic length (l_m), wire count (N), and wire size (SWG: Standard Wire Guage), Section 5, meticulously explored the reliability and failure rates of the power components by providing insights into the failure rate, mean time to failure (MTTF), and various influencing factors. Moving forward, Section 6 navigates through the assessment of failure rates for power components, dissecting elements such as base failure rate, temperature, quality, environment, and application factors, Section 7 discusses the results related to inductor design, power loss analysis of power components and showcase the results related to reliability, failure rate, further Section 8 summarizes the key findings and the paper concludes with a comprehensive reference section.

2. Physical Significance of Inductor in Transformerless DC-DC Boost Converter

The magnetic component i.e. inductor also known as the 'heart' of a converter, plays a significant role in transformerless DC-DC boost converters. These components are essential for attaining higher voltage levels and facilitating efficient power conversion across a variety of electronic applications [15]. One of the primary functions of the inductor is to elevate the output side voltage level from a lower input voltage. The inductor 'L' accumulates energy within its magnetic field during the switch's on-time phase and discharges it during the off-time, which increases the output voltage. Additionally, inductors convert electrical energy into a magnetic field, which is subsequently delivered to the output once the switch is turned off. This energy transfer facilitates voltage elevation without the need for large, expensive transformers, making transformerless boost converters more compact and economical.

In some scenarios, providing isolation is essential for safeguarding the circuit. [15-17], [23], [29], [34]. While transformerless boost converters do not employ traditional transformers for isolation, they can still provide some degree of electrical isolation through the use of coupled Inductors or other magnetic components.

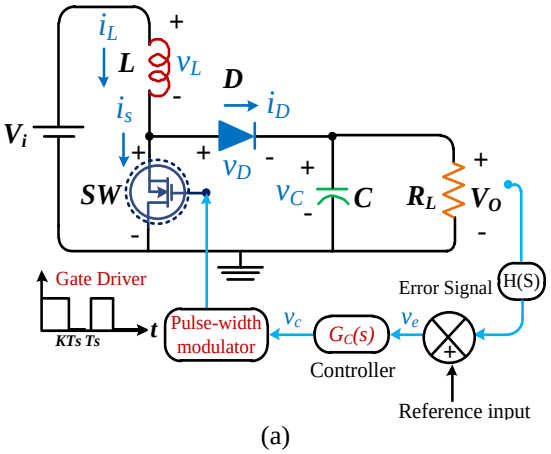
This isolation helps prevent ground loop issues and ensures the safety of sensitive electronic components. Inductors help in reducing power losses in the converter by storing and transferring energy efficiently. Thus it enhanced the overall efficiency of the boost converter, making it an attractive choice for battery-powered devices and energy-efficient systems. Transformerless boost converters benefit from the compact size and reduced weight of the inductor compared to traditional transformers.

3. Transformerless DC-DC Boost Converter

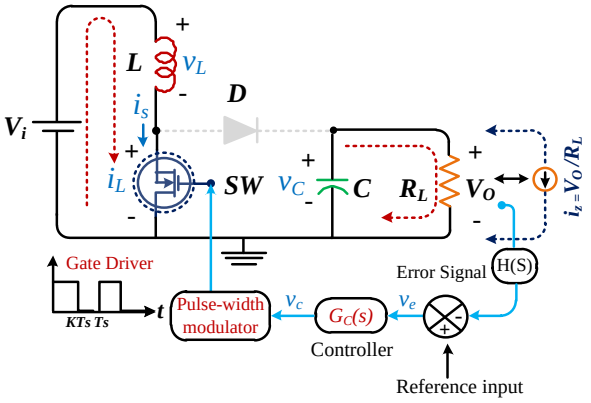
To comprehend the operation of this converter, bi-switching scenarios, first, when the switch is 'ON' and another when the switch is OFF, have been utilized. A boost is a specific kind of DC-DC converter designed to raise a lower voltage input to produce a higher voltage output as shown in Fig. 3(a). It achieves this through a switching process controlled by a semiconductor switch, typically a MOSFET transistor, and an energy-storage component, such as an Inductor.

To initiate the process of voltage conversion, the MOSFET is turned on during a time interval of $(0 < t \leq KT)$ or KT as illustrated in Fig. 3(b). During this instant, it connects the supply voltage (V_i) to the inductor (L). When the MOSFET is in the 'ON' condition, the voltage across the diode is equal to '-V_o' as shown in Fig. 3(d). Due to this, the diode is turned off by reverse biasing i.e. diode current (i_D) become zero. Further, the current flows linearly with a slope of $'V_i/L'$ through the inductor, accumulating energy in its magnetic field as shown in Fig. 3(d). During this instant $'v_L'$ for the current to circulate to the load, forming a closed loop. The output voltage (V_o) is also present across the capacitor and load, although it is lower than the intended output voltage.

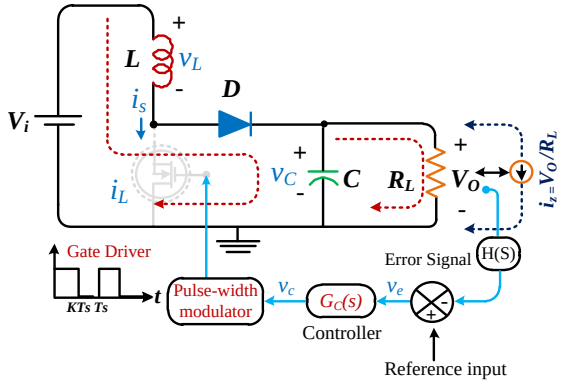
Further, at interval $(KT< t \leq tT)$ or $(1-K)T$, the MOSFET becomes 'OFF' [refer Fig.3(c)]. İt collapsed the



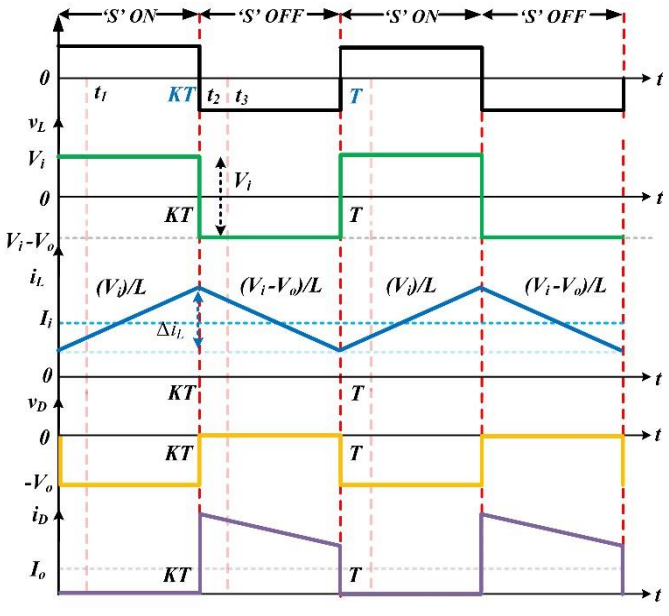
(a)



(b)



(c)



(d)

Fig. 3. Boost converter & its switching states waveform (a) closed loop structure of converter (b) State I: Switch: close (c) State II: Switch: open (d) Principle waveform $'v_L'$, $'i_L'$, $'v_D'$, & $'i_D'$.

inductor magnetic field. The collapsed inductor's magnetic field leads to a variation in the current flow. The variation in current generates a voltage across the inductor, denoted as $'v_L'$, which equals $(V_i - V_o)$, but is oriented in the opposite direction to the input voltage. Consequently, this leads to a decrease in the inductor current at a rate of $(V_i - V_o)/L$. In this state, the inductor discharges its accumulated energy. The energy is transferred towards the output through the diode which becomes forward-biased. As the current flows, it charges the output capacitor, helping to maintain a steady voltage. This process ensures that the load receives a continuous supply of energy. Additionally, the efficiency of this energy transfer is crucial for the overall performance of the DC-DC boost converter. The diode allows current to flow from the inductor (L) to the output capacitor (C) and the load (R). This process increases the output voltage (V_o) beyond the input voltage (V_i), effectively reaching the target voltage level. The boost converter continually cycles through these switching states, using the duty cycle to drive the output voltage. So in this way inductor plays an important role in By modifying the duty cycle, it is possible to regulate the output voltage to the desired level. The duty cycle 'K' of the Boost converter is depicted as Eq. (1):

$$K = 1 - \frac{V_i}{V_o} \tag{1}$$

Ripple current $'\Delta i_L'$, inductance and capacitance have been evaluated using Eq. (2), (3), & (4).

$$\Delta i_L = \frac{K * V_0 * (-K + 1)}{L * f_s} \tag{2}$$

The inductor 'L' value has been calculated as [refer Eq. (3)]:

$$L = \frac{R_L * (1 - K)^2 * K}{2 * f_s} \tag{3}$$

Further, the value of capacitor 'C' has been calculated as [refer Eq. (4)]:

$$C = \frac{K * V_0}{f_s * R_L * V_{C_{Peak}}} \tag{4}$$

Similarly, the power losses 'P_{loss}' and efficiency $'\eta'$ are estimated using Eq. (5) & (6) respectively:

$$P_{Loss} = \sum \text{power loss across each component} \tag{5}$$

$$'\eta' = \frac{P_O}{P_O + P_{Loss}} \tag{6}$$

$$\left.\begin{aligned} \begin{bmatrix} \dot{i_L} \\ \dot{v_C} \end{bmatrix} &= \begin{bmatrix} 0 & -\frac{(-k+1)}{L} \\ \frac{(-k+1)}{C} & -\frac{1}{CR} \end{bmatrix} \begin{bmatrix} i_L \\ v_C \end{bmatrix} + \begin{bmatrix} \frac{1}{L} \\ 0 \end{bmatrix} v_i + \begin{bmatrix} 0 \\ -\frac{1}{C} \end{bmatrix} i_z \\ \begin{bmatrix} v_O \\ i_i \end{bmatrix} &= \begin{bmatrix} 0 & 1 \\ 1 & 0 \end{bmatrix} \begin{bmatrix} i_L \\ v_C \end{bmatrix} \end{aligned}\right\} \tag{7}$$

$$\left.\begin{aligned}\begin{bmatrix}\dot{0}\\ 0\end{bmatrix} &= \begin{bmatrix}0 & -\frac{(-k+1)}{L}\\ \frac{(-k+1)}{C} & -\frac{1}{CR}\end{bmatrix}\begin{bmatrix}I_L\\ V_C\end{bmatrix} + \begin{bmatrix}\frac{1}{L}\\ 0\end{bmatrix}V_i + \begin{bmatrix}0\\ -\frac{1}{C}\end{bmatrix}I_z\\ \begin{bmatrix}V_O\\ I_i\end{bmatrix} &= \begin{bmatrix}0 & 1\\ 1 & 0\end{bmatrix}\begin{bmatrix}I_L\\ V_C\end{bmatrix}\end{aligned}\right\} \quad (8)$$

$$\left.\begin{aligned}\begin{bmatrix}\dot{\hat{\imath}}_L\\ \dot{\hat{v}}_c\end{bmatrix} &= \begin{bmatrix}0 & -\frac{(1-k)}{L}\\ \frac{(1-k)}{C} & -\frac{1}{CR}\end{bmatrix}\begin{bmatrix}\hat{\imath}_L\\ \hat{v}_c\end{bmatrix}\\ &+ \begin{bmatrix}\frac{1}{L} & 0 & \frac{V_o}{L}\\ 0 & -\frac{1}{C} & -\frac{I_L}{C}\end{bmatrix}\begin{bmatrix}\hat{v}_i\\ \hat{\imath}_z\\ \hat{k}\end{bmatrix}\\ and\ \begin{bmatrix}\hat{v}_o\\ \hat{\imath}_i\end{bmatrix} &= \begin{bmatrix}0 & 1\\ 1 & 0\end{bmatrix}\begin{bmatrix}\hat{\imath}_L\\ \hat{v}_c\end{bmatrix}\end{aligned}\right\} \quad (9)$$

Further, the different analytical control models have been obtained through dynamic modeling and expressed as Eq. (7) to Eq. (9) respectively.

4. Design of an Inductor in 12 V to 24 V Transformerless DC-DC Boost Converter

An inductor is a fundamental element in the electronic circuit (in the context of a boost converter), playing a crucial role in energy storage, filtering, and signal conditioning. Proper inductor design is essential to ensure optimal performance in various applications, such as power supplies, voltage regulators, and electromagnetic interference (EMI) filters. Figure 4, shows the toroidal structure of inductor.

The design and selection process of L employs the *'Area Product Method (APM),'* a structured approach that determines the appropriate core size and number of windings to meet specified performance requirements such as inductance, current handling capacity, and efficiency [14]. Physically, an inductor comprises a coil wound around a magnetizing core. The core possesses several properties, including its ability to attract magnetic fields (magnetic flux density or B_m), the dimensions of its cross-section (A_{CS}), area of its 'W_A', the extent of its magnetic effect (magnetic length, 'l_m'), its response to magnetic fields (permeability or 'μ').

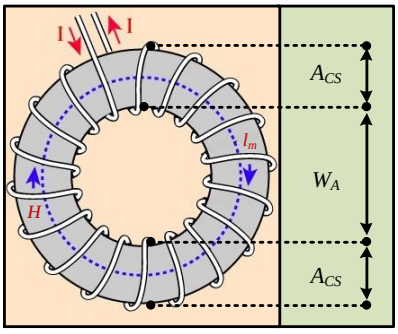


Fig. 4. Structure of inductor in toroidal form.

During the inductor design process, the relationship between these electrical and magnetic parameters is crucial for selecting the core material, determining the coil wire thickness, calculating the number of windings (N), and deciding whether to include an air gap. The toroidal form of the inductor is shown in Figure 4. The 'Area Product Method' systematically assists in designing inductors for switching power supplies by offering insights into critical factors like window area (W_A), core cross-sectional area ($\boldsymbol{A_{CS}}$), number of turns (N), wire size, and core material selection.

4.1 Assessment of Area of Window ($\boldsymbol{W_A}$)

Let "*a*" represent the cross-sectional wire area and *"N"* stands for turns count. This relationship between these variables is expressed as Eq. (10).

$$(W_k) * (W_A) = \frac{(N) * (I_{rms})}{J} \quad (10)$$

Where, 'W_k' is called the *'utilization factor of the window'* and 'J' represents the current density in A/m^2.

The maximum current 'I_m' along with the rms 'I_{rms}' of the i_L is determined by the crest factor 'C_K' as expressed in Eq. (11), which characterizes the shape of the current waveform [24].

$$C_K = {I_m}/{I_{rms}} \quad (11)$$

From Eq. (10) & Eq. (11), the Window area can be achieved using Eq. (12).

$$W_A = \frac{(W_K) * (C_K) * (I_{rms}) * (N)}{J} \quad (12)$$

4.2 Assessment of Area Product ($\boldsymbol{A_P}$)

As per Faraday's law

$$e = L * \frac{di}{dt} = A_{CS} * \frac{dB}{dt} * N \quad (13)$$

On integrating Eq. (13), we have

$$L * I_m = N * B_m * A_{CS} \quad (14)$$

Here, B_m : maximum flux density in the core, I_m : maximum windings current.

When an electric current passes inductor energy is accumulated and represented as Eq. (15).

$$E_L = \frac{1}{2} * L * {I_m}^2 \quad (15)$$

So from Eq. (10) and (11), 'A_P' is expressed as Eq. (16).

$$A_P = \frac{2 * E_L}{(C_K) * (W_K) * J * B_m} \quad (16)$$

Here, $'J'$ is termed as the current density and denoted in A/m^2.

5. Reliability and Failure Rates

Reliability is defined as the capacity of a system, to consistently execute its designated function under specified conditions for a particular period of time. The process of assessing reliability involves examining the probability of failures & their frequency, and other critical factors to confirm that the system performs as expected. This is commonly depicted through a model called the 'Reliability function,' symbolized as $\mathbb{R}(t)$ [19]. This calculates the likelihood that a system will function without failure during a specified time interval, [0, t]. Essentially, $\mathbb{R}(t)$ is an expression that describes the ability to maintain reliable operation over a given period [17-20].

5.1. Failure Rate

It is a key metric used to assess reliability in different areas like electronics and quality management. It represents the likelihood that a system or component will experience failure over a given time frame. The failure rate can be measured in failures/Hrs, failures/10^6Hrs, or failures/10^9 Hrs, as per need. It is commonly described in two forms: the instantaneous failure rate (λ) and the time-dependent failure rate [λ(t)].

- The λ, reflects the chances that a component or system will fail within an extremely short period. This measure is continuous, typically expressed as failures per time unit, indicating the rate of failure at any specific moment. Reliability models, such as the exponential distribution, often utilize 'λ' to estimate the likelihood of failure at a particular point in time. This rate can change, especially in systems where wear and tear affect performance over time.
- The time-based rate of failure, represented as 'λ(t),' provides an estimate of the number of failures occurring over a specific period. Unlike the continuous form of the instantaneous rate, λ(t) applies to discrete time periods, often reported in failures per hour or another time unit (e.g., λ(t) failures per 1,000 hours). This metric helps determine the likelihood of failure and is useful for evaluating the reliability of a system or component over time. While 'λ' offers a snapshot at any given time, 'λ(t)' gives insight into the failure rate across distinct intervals. The '$\lambda(t)$' is depicted in Eq. (17).

The ' $\mathbb{R}(t)$' denotes the chances of uninterrupted operation without encountering failure, characterized by Eq. (18).

$$\lambda(t)\cdot = -\frac{d}{dt}[\mathbb{R}(t)] \tag{17}$$

$$\mathbb{R}(t) = e^{-\int_0^t \lambda(t)dt} \tag{18}$$

5.2. Mean Time to Failure (MTTF)

It illustrates the time of component operates before experiencing its first failure. It is a crucial measurement of reliability and is typically given in units such as hours (Hrs)/days/years. From a mathematical perspective, it is expressed as the integral of the system's lifespan, which is calculated using, $\mathbb{R}(t)$ expressed as Eq. (19).

$$MTTF = \int_0^{+\infty} \mathbb{R}(t) \tag{19}$$

When the $\lambda(t)$ remains constant with time, the MTTF can be estimated as the inverse of λ, as stated in Eq. (20) [24].

$$MTTF = \frac{1}{\lambda} \tag{20}$$

6. Assessment of Failure Rates of Power Components in 12 V to 24 V Boost Converter

The reliability assessment model comprises failure rates and stress factors. İt represents a fundamental framework within the domain of engineering and system analysis, offering a comprehensive approach to understanding the performance of components or systems over time. At its core, this model integrates two essential elements: failure rates and stress factors. The interplay between these components forms the basis for evaluating and predicting the reliability of a given system or component under various operating conditions and environmental stresses.

6.1. The Base Failure Rate (λ_B)

It is often expressed as (λ_B), serves as a key metric. It signifies the failures over a specific time when subjected to particular operating conditions. conditions. This rate reflects the initial likelihood of failure before any external factors or aging come into play. The base failure rate is mathematically defined as the failure rate measured when stress factors—such as temperature, voltage, and environmental conditions—are maintained at their standard or nominal levels, as outlined in Eq. (21) [24]. This provides a reference for evaluating how components or systems perform under ideal operating conditions.

$$\lambda_B = \lim_{\Delta t \to 0}[\{F(t+\Delta t) - F(t)\}/\Delta t] \tag{21}$$

Here, '*F(t)*' represents the failure time's distribution function.

6.2. Temperature Factor (π_T)

Temperature stands as a crucial environmental factor that affects the reliability and life of electronic components, systems, and various industrial equipment [24]. In reliability assessment, the temperature factor, commonly represented as $'\pi_T'$, perform a substantial role in quantifying the influence of temperature fluctuations on failure rates. It is also used to modify the initial failure rate of a component or system by taking into account the effects of operating temperature.

6.3. Quality Factor (π_Q)

It is the measure of quality, expressed as $'\pi_Q'$, represents a comprehensive metric that evaluates various aspects of quality. This quality factor is crucial for assessing the reliability of electronic components by evaluating the impact

of design, materials, and operating conditions on failure rates. π_Q quantifies the reliability improvement resulting from these factors, often incorporating elements such as temperature, electrical stress, and mechanical stress into its calculation. The primary purpose of π_Q is to adjust the base failure rate according to the quality of the components and design choices, enabling better prediction and enhancing the reliability of boost converters throughout their operational lifespan.

6.4. Environment Factor (π_E)

The environmental factor plays a key role in assessing. reliability. It tells about the environment that can significantly as temperature, humidity, vibration, shock, etc. In reliability engineering, this factor is crucial because the conditions in which a component operates—such as exposure, radiation, dust, electromagnetic interference (EMI), and altitude—can profoundly impact its overall reliability, durability, and expected service life.

6.5. Application Factor (π_A)

The application factor, often depicted as $'\pi_A'$ is a parameter used in reliability engineering to account for the specific operating conditions or stresses that a system or component may experience during its lifecycle This factor is applied to the basic life or reliability data of a component to adjust for the effects of these conditions. The specific form of the application factor may vary depending on the context and the type of stress or condition being considered in reliability analysis. As the boost converter mainly contains power elements like a MOSFET, diode, inductor & capacitor, and resistor in its circuit, Table 1 and Table 2 provide important information related to failure rates [24]. Table 1 systematically depicts the individual expressions of part failure rates and their respective temperature factors, spanning a spectrum of power components, including switches, diodes, resistors, capacitors, and inductors.

Each expression provides important help in analyzing the relationship between operating temperature, environmental conditions, and the inherent characteristics of each component. Meanwhile, Table 2 delves into the thermal dynamics of these components, offering insights into hot spot temperatures for inductors, junction-to-ambient & junction temperatures. Additionally, the table elucidates power losses for each power component, providing a comprehensive understanding of how energy is dissipated within the system. The inclusion of electrical stress factor formulas for diodes, capacitors, and resistors further enhance the scope of this analysis. Military handbook 217F has been utilized for analyzing factors of temperature, environment, and quality [21]. Tables 1 and 2 provide a robust foundation for the analysis and prediction of component failure rates, thermal behavior, and power dissipation in electronic systems.

7. Results & Discussion

In the transformerless version of a boost converter, the magnetic energy storage element performs an important part as explained in section 2. To evaluate the inductor's value and its behavior & performance, a 12 V to 24 V, 2 A DC-DC boost converter has been designed that is operated at 100 kHz switching frequency. Duty cycle '*K*' has been evaluated as 50% through Eq. (1). Before obtaining the value of an inductor, the converter ripple current which is denoted by $'\Delta i_L'$, has been calculated as 8 A through Eq. (2). Further, the values of the inductor and capacitor have been calculated as 7.5 µH and 83.33 µF respectively at 100 kHz.

In the same fashion, the values of the inductor and capacitor have been calculated at 500 kHz as 1.5 µH and 16.66 µF respectively. Further, an STD15N10T4 FET switch has been selected that have V_{Dss} of 100 V, I_D of 23 A, and R_{Ds} of 65 $m\Omega$. Further, the RB238T60NZ Schottky diode has been chosen that further have I_D of 40 A, V_{RM} of 60 V, and a forward voltage of 0.86 V. At this stage the understanding of datasheets play an crucial role to estimate the reliability, as a wrong selection can create uncertainities in results.

Table 1. Failure rates (in failure / 10^6 Hrs.) of power components (λ_P : part failure rates, π_T : Temperature factor, λ_B : failure rate (base), π_E : factor of environmental, π_Q: factor of quality, T_{Hs}: hot-spot temperature (℃), T_A : ambient temperature (℃), Θ_{JA} : thermal resistance (junction-to-ambient), Θ_{JC} : thermal resistance (junction-to-case in °C/W), π_A : application factor, π_C : Factor of construction, π_{SR} : factor of series resistance, E_a : activation energy, T_{RC} : case temperature of the resistor) [18][21].

Elements	λ_P	π_T
Inductor '*L*'	$\lambda_{P_L} = (\lambda_B) * (\pi_T) * (\pi_E) * (\pi_Q)$	$\pi_T = \exp\left\{(-1276.5463) * \left(\frac{1}{T_{Hs}+273} - \frac{1}{298}\right)\right\}$
Diode '*D*'	$\lambda_{P_D} = (\lambda_B) * (\pi_T) * (\pi_E) * (\pi_Q) * (\pi_S) * (\pi_C)$	$\pi_T = \exp\left\{(-3091) * \left(\frac{1}{(T_A + \Theta_{JA}P_{loss}) + 273} - \frac{1}{298}\right)\right\}$
Capacitor '*C*'	$\lambda_{P_C} = (\lambda_B) * (\pi_T) * (\pi_E) * (\pi_Q) * (\pi_V) * (\pi_c) * (\pi_{SR})$	$\pi_T = \exp\left\{(-11604.97 * E_a) * \left(\frac{1}{(T_C + 273} - \frac{1}{298}\right)\right\}$
Switch '*SW*'	$\lambda_{P_{SW}} = (\lambda_B) * (\pi_T) * (\pi_E) * (\pi_Q) * (\pi_A)$	$\pi_T = \exp\left\{(-1925) * \left(\frac{1}{(T_A + \Theta_{JC}P_{loss}) + 273} - \frac{1}{298}\right)\right\}$
Resistor '*R*'	$\lambda_{P_R} = (\lambda_B) * (\pi_T) * (\pi_E) * (\pi_Q) * (\pi_P) * (\pi_S)$	$\pi_T = \exp\left\{(-11604.97 * E_a) * \left(\frac{1}{(T_{RC} + 273)} - \frac{1}{298}\right)\right\}$

Table 2. Expression for various power losses, thermal resistance, temperatures, and stress factors (P_{V_F} **:** loss due to forward voltage**,** P_{R_F} : loss due to forward resistive voltage, T_J : junction temperature, T_A : ambient temperature) [18][21].

Elements	Respective T_{Hs} / Θ_{JA} / T_C / Θ_{JC} / T_{RC}	Power Losses (P_{loss})	Elec. Stress factors
Inductor '*L*'	$T_{Hs} = \{T_A + (1.1) * (\Delta T)\}$	$P_{loss} = r_L * I_{L_{rms}}^2$	-
Diode '*D*'	$\Theta_{JA} = \{(T_J - T_A)/P_{loss}\}$	$P_{loss} = P_{V_F} + P_{R_F}$	$\pi_S = (V_s)^{2.43}$
Capacitor '*C*'	$T_C = \{T_A + (\Theta_{JA} * P_{loss})\}$	$P_{loss} = r_c * I_{C_{rms}}^2$	$\pi_v = V_{O(operating)}/V_{R(rated)}$
Switch '*SW*'	$\Theta_{JC} = \{(T_J - T_A)/P_{loss}\}$	$P_{loss} = \{P_{r_{DS}} + (P_{sw} / 2)\}$	-
Resistor '*R*'	$T_{RC} = \{T_A + (\Theta_{JA} * P_{loss})\}$	$P_{loss} = R * I_o{}^2$ or V^2/R	$\pi_S = (e)^{\{(1.1)*(s)\}}$

7.1. Design of an Inductor in a 12 V to 24 V DC-DC Boost Converter

The inductor was designed using the Area Product Method (APM). To identify key parameters like W_k, C_K, and energy accumulated in L (E_L), have been obtained using Eq. (10),(11) & (15) as W_k of 0.6, C_K of 4 and E_L of 240×10^{-6} $jule$ respectively. The area product (A_P) has been evaluated using Eq. (16) which provides A_P=0.0267 cm^4 via selecting the flux density 'B_m' = 0.25 and $J = 3 \times 10^6$ A/m^2. The T44-26 toroidal iron powder core has been selected for the design of the inductor. The selected core exhibits A_P of $0.0267cm^4$, W_A of 0.266 cm^2, C_A of 0.099 cm^2, and l_m of 2.68 cm. Likewise, for operation at 500 kHz, a toroidal iron powder core (T30-26) [14] has been identified. This specific core demonstrates an A_P of $0.0070cm^4$, W_A of 0.116 cm^2, and C_A of 0.06 cm^2. Additionally, to calculate the turns count and the wire area, it is necessary to determine the permeance. Permeance ($\mathcal{P}$) is an important factor that indicates how readily magnetic flux can form within a material or magnetic circuit. It is calculated using Eq. (22).

$$(\mathcal{P}) = \frac{\mu_0 * C_A * \mu_r}{(\mu_r * l_g) + l_m} \text{ H/}Turn^2 \tag{22}$$

Here, μ_0=free space permeability, μ_r = relative permeability, l_g= air gap length (in m), 'l_m' is the magnetic path length of core (m), 'C_A' = core's cross-sectional area (m^2). Further to obtain the number of turns and wire gauge selection Eq.(23) has been utilized.

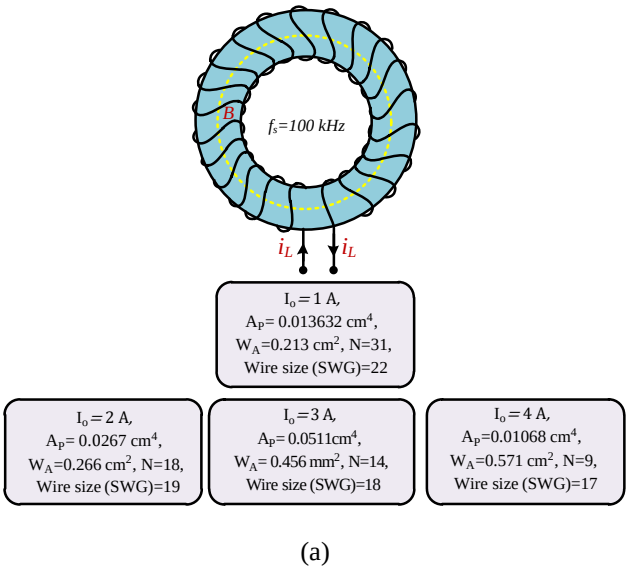
$$\left.\begin{aligned} N &= \sqrt{L/\mathcal{P}} \\ a &= \frac{Irms}{J} mm^2 \end{aligned}\right\} \tag{23}$$

Based on Eq. (22) and (23), the turn count and size of the wire has been estimated. The results indicate that at a frequency of 100 kHz, the inductor requires 18 rounds with 19 SWG wires. Similarly, at another frequency, the inductor requires 10 rounds with 19 SWG wires.

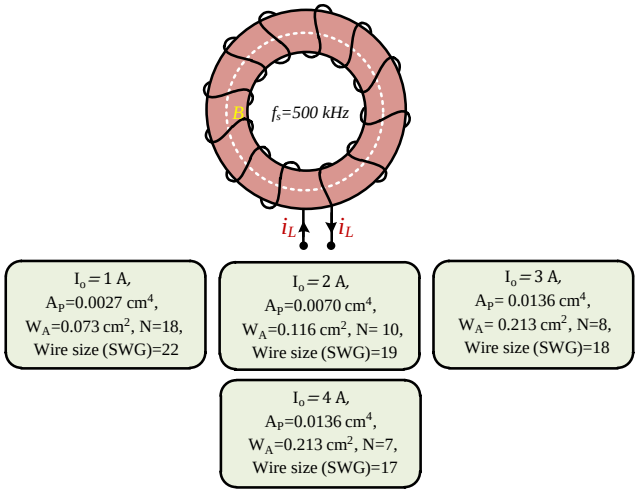
The analysis has been carried out through Eq. (10) to (16) and Eq. (22) & (23) across 1 to 4 A of output currents. Figure 5 shows the design observations of the inductor for a transformerless boost converter, which clearly depicts that with an increase in output current, both the area product (A_P) & window area (W_A) of the inductor increases together. Additionally, it has also been observed that as the current value escalates from 1 to 4A, the number of turns diminishes and there is a corresponding reduction in the wire size, measured in terms of 'SWG' (Standard Wire Gauge).

In Fig. 5(a) & 5(b), toroidal cores have been depicted that show the parameters like *N*, SWG, and A_P. The operational characteristics of the inductor have been assessed at multiple frequencies, as illustrated in Fig. 5(c), 5(d), 5(e), and 5(f) in terms of dimensions (cross-section, window, and wire) and turn counts respectively. The results reveal that at elevated switching frequencies, the size of the inductor diminishes when compared to its dimensions at 100 kHz, consequently leading to a reduction in the core size. As a result, to design a inductor for 12V to 24V at 2A converter a iron powder core (T44-26) with A_P of 0.0267cm^4, W_A of 0.266 cm^2, C_A of 0.099 cm^2, and l_m of 2.68 cm which needs 18 numbers of rounds with 19 SWG of wire, required.

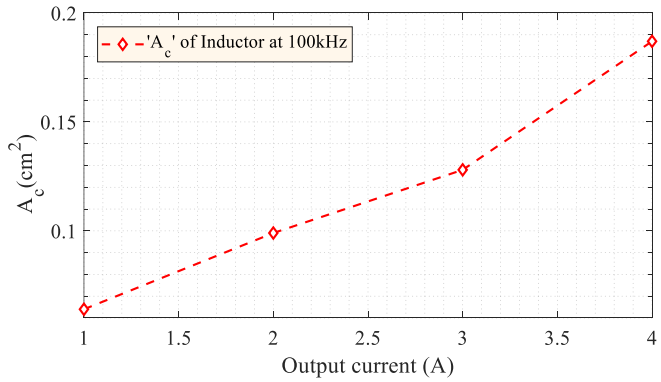
The analysis of the inductor has been exhaustively conducted across a spectrum of input voltage & load scenerio to characterize its behavior at both frequencies. Figure 6 illustrates the performance analysis of the inductor with reference to the output current [Fig. 6(a)] and load resistance [Fig. 6(b)] at fixed input voltages (8 V, 12 V and 16 V) conditions.



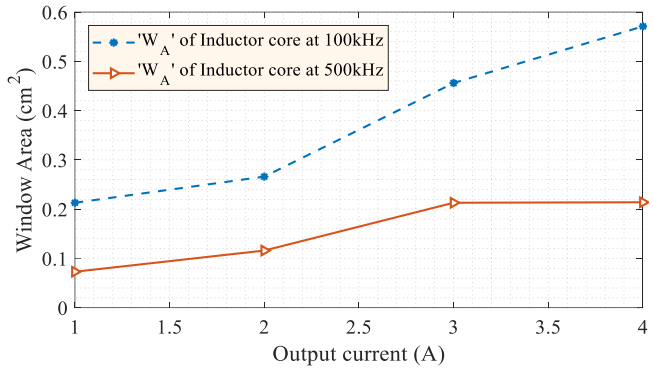
(a)



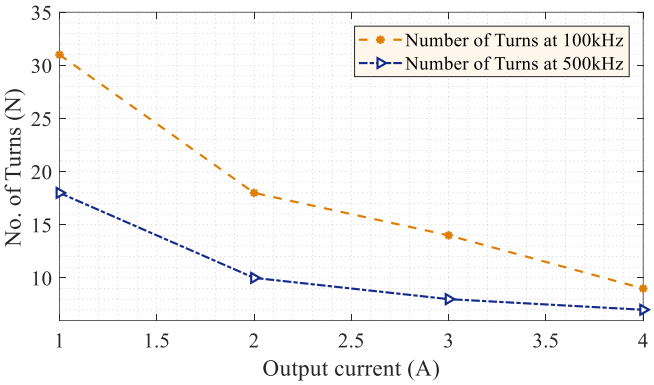
(b)



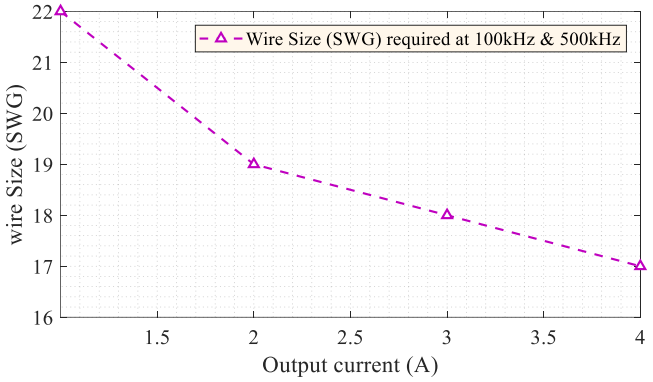
(c)



(d)



(e)

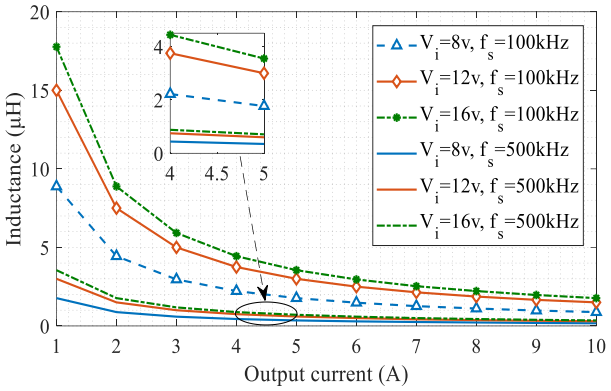


(f)

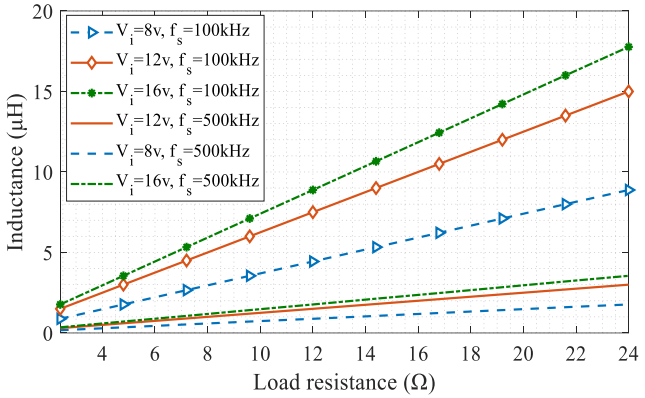
Fig.5. Design results of the inductor in 12V to 24V transformerless boost converter (a) Inductor design at f_s=100 kHz (b) inductor design at f_s=500 kHz (c) cross-sectional area with reference to I_o at 100 kHz (d) window area as a function of I_o at 100 & 500 kHz (e) 'N' vs I_o at 100 & 500 kHz (f) size of wire (SWG) vs I_o.

At 100 kHz, it is apparent that an increment in output current results in a decrement in inductance. Further, the analysis that has been carried out under varying load conditions reveals that as the load changes, the inductance also experiences the change. The responses have also been scrutinized at 500 kHz, indicating that at higher frequencies, the necessary inductance is lower, leading to a consequential reduction in core size. Understanding and analyzing the power losses in MOSFET, diode, inductors, and capacitors, is

integral to the design and reliability of electronic systems, particularly in power electronics.



(a)



(b)

Fig. 6. Performance evaluation of inductor at frequencies of 100 and 500 kHz, at fixed V_i of 8v, 12v, & 16v illustrating: (a) response in relation to I_o (b) response in relation to R_L.

7.2. Analysis of Inductor's Behavior Through Assessment of Power Losses Including FET, Diode, and Capacitor

Power losses, often manifested as heat dissipation, can significantly impact the efficiency and overall performance of these components. Power losses in electronic components can occur due to parasitic elements, which are unintended and often inherent in the components or the overall circuit. Parasitic elements include resistances, inductances, capacitances, and stray elements that are not part of the intended design but affect the performance of the circuit. Figure 7 illustrates the equivalent circuit of a transformerless DC-DC boost converter with parasitic elements (r_L, r_C, r_{Ds}).

In this section, the behavior and performance of the inductor in a 12 V to 24 V transformerless DC-DC boost converter have been assessed through power loss analysis using the Matlab® Simulatio platform. The power losses can be calculated using the formulas depicted in Table 2. To comprehensively assess the inductor's performance, it is essential to simultaneously analyze these losses for other vital power components such as the FET, diode & capacitor. The analysis of these losses encompasses the impact of I_o and R_L.

Figure 8, shows the power loss analysis of the switch(MOSFET) in a 12 V to 24 V boost converter. The

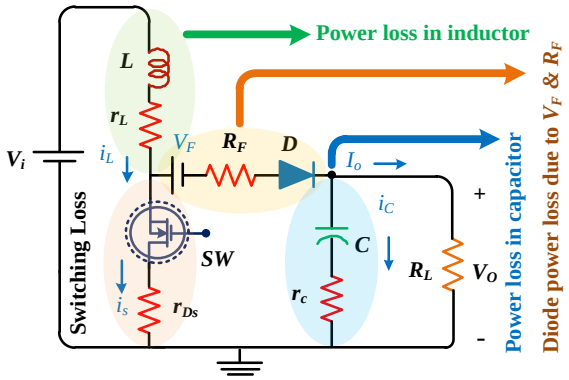
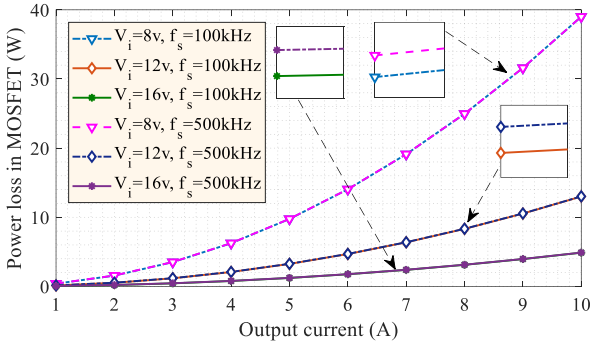
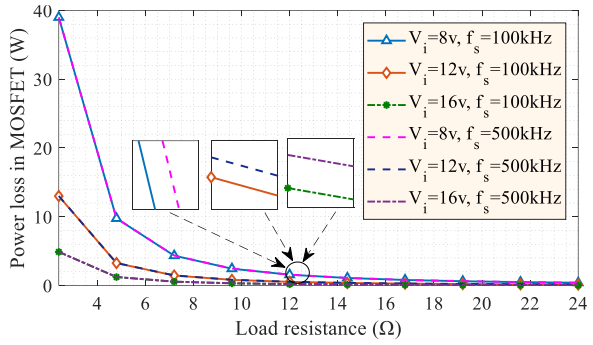


Fig. 7. Transformerless DC-DC boost converter with parasitic elements



(a)



(b)

Fig. 8. Power loss analysis of switch at 100 and 500 kHz at fixed values of V_i=8v, 12v, and 16v illustrating: (a) response relative to I_o (b) response in relation to R_L

power losses in the MOSFET of the boost converter have been analyzed under different fixed input voltage conditions (V_i=8 V, 12 V & 16 V) for varying output currents ranging from 1 to 10 A at 100 & 500 kHz frequencies as shown in Fig. 8(a).

At V_i = 8 V, the power losses increased progressively from 0.3936 W at 1 A to 39.0036 W at 10 A. At V_i=12 V, the losses ranged from 0.1336 W at 1 A to 13.0036 W at 10 A. Similarly, at V_i=16 V, the power losses again increase from 0.0534 W at 1 A to 4.8786 W at 10 A.

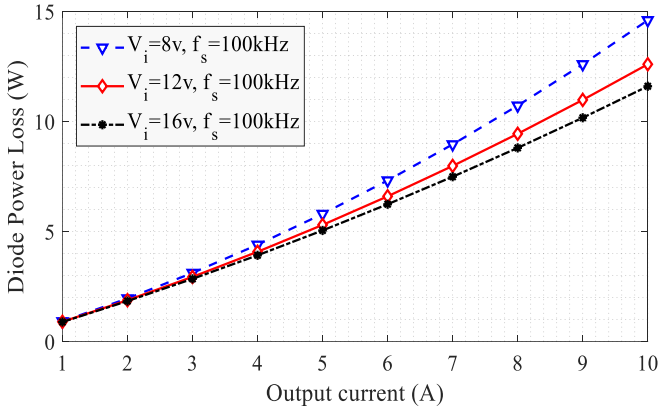
Results also showcase that at higher switching frequency the power loss shows an increment. From these observations, it is clear that power losses in switches are increasing with varying (increase) output current and higher switching frequencies.

Further, the power losses in the MOSFET of the boost converter have been investigated across a spectrum of load resistances, specifically 2.4 ohms to 24 ohms under different fixed input voltage conditions ($V_i = 8$ V, 12 V, and 16V) at 100 & 500 kHz frequencies as shown in Fig. 8(b). At $V_i = 8$ V, the power losses showcase a consistent decreasing trend with increasing load resistance, ranging from 39.0036 W at 2.4 ohms to 0.3936 W at 24 ohms.

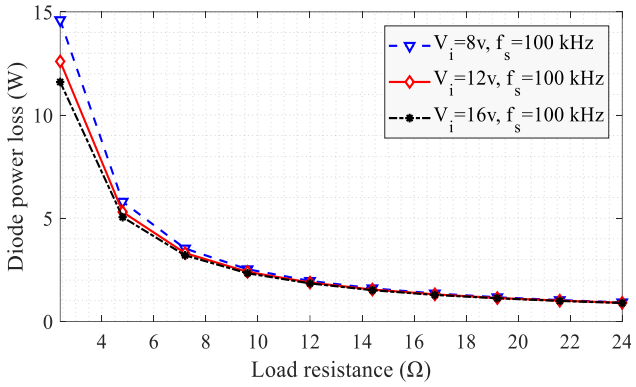
At $V_i = 12$V, the losses were decreased as the load resistance increased, varying from 13.0036 W at 2.4 ohms to 0.1336 W at 24 ohms. Notably, at $V_i = 16$ V, the power losses exhibited a similar pattern, decreasing from 4.8786W at 2.4 ohms to 0.0524W at 24 ohms. These results indicate that higher load resistances contribute to reduced power losses in the MOSFET, showcasing a favorable trend for improved efficiency. The inverse relationship between load resistance and power losses aligns with expectations, where higher load resistances lead to lower current flow and, consequently, diminished losses. At higher switching frequencies the power losses have been observed more sensitive in comparison to 100 kHz.

Further, Fig. 9, shows the power loss investigations of the diode in a 12 V to 24 V boost converter. These losses of diode have been analyzed under different fixed input voltage conditions ($V_i = 8$ V, 12 V, and 16 V) at 100 kHz frequency. At an input voltage (V_i) of 8 V, the diode losses increase gradually from 0.92 W at 1 A to 14.6 W at 10 A. Similarly, at 12 V input, the losses range from 0.9 W to 12.6 W, and at 16V input, they vary from 0.89 W to 11.6 W as shown in Fig. 9(a).

The observed trend suggests that diode losses generally escalate with increasing output current, irrespective of the input voltage. This behavior is expected as higher output currents result in elevated conduction losses in the diode due to increased forward current. The influence of input voltage is also evident, with lower losses observed at higher input voltages for a given output current. This can be attributed to the reduced voltage drop across the diode at higher input voltages, contributing to lower conduction losses.



(a)



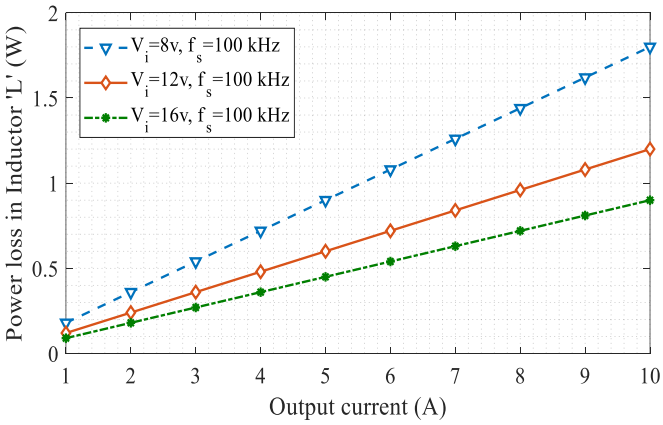
(b)

Fig. 9. Power loss analysis of Schottky diode at 100 kHz at fixed values of V_i= 8v, 12v, and 16v illustrating: (a) response relative to I_o (b) response in relation to R_L .

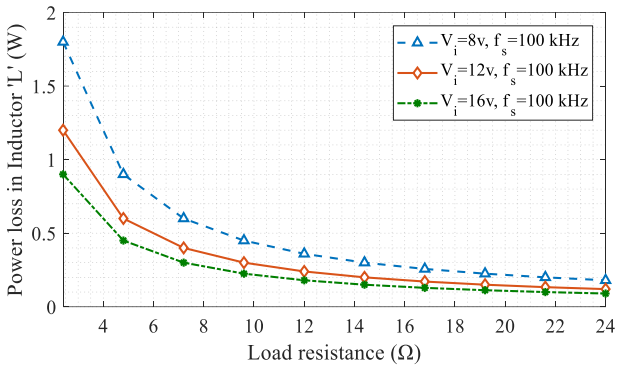
Further, the power losses in the diode of the boost converter have been investigated across varying load conditions, specifically 2.4 ohms to 24 ohms under different fixed input voltage conditions (8 V, 12 V, & 16V) at 100 kHz frequency as shown in Fig. 9(b). At $V_i = 8$ V, the power losses showcase a consistent decreasing trend ranging from 14.60 W at 2.4 ohms to 0.92 W at 24 ohms. Further, at $V_i = 12$ V, the power losses again showcase a consistent decrease from 12.60 W at 2.4 ohms to 0.90 W at 24 ohms. Similarly, at $V_i = 16$ V, the power losses again showcase a consistent decrement from 11.60 W at 2.4 ohms to 0.89 W at 24 ohms. The results show that higher load resistances lead to reduced diode losses, which aligns with the expected behavior in a boost converter. Higher load resistances result in lower diode currents during the freewheeling phase, contributing to decreased conduction losses.

Figure 10, shows the power loss investigations of the inductor in a 12 V to 24 V boost converter at 100 kHz frequency. Analyzing the power losses in the inductor provides valuable insights into its behavior. At an input voltage of 8V, inductor losses increase gradually with higher output currents, ranging from 0.18 W at 1 A to 1.8 W at 10A as shown in Fig. 10(a).

Similarly, at 12V input, inductor losses follow a similar pattern, increasing from 0.12 W to 1.2 W with rising output



(a)

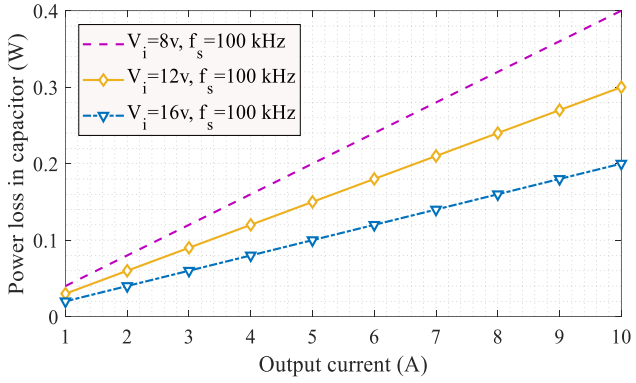


(b)

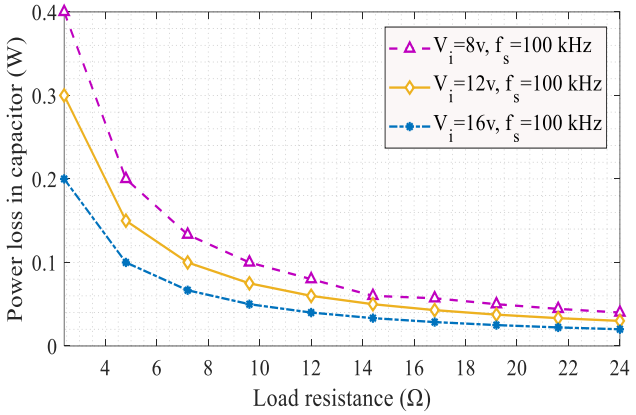
Fig. 10. Power loss analysis of inductor at 100 kHz frequency at V_i= 8V, 12V, and 16V illustrating: (a) response related to the output current and (b) response related to load resistance.

current. At 16 V input, the inductor losses continue to exhibit a proportional increase, varying from 0.09 W to 0.9 W. The observed trend suggests that inductor losses are directly proportional to the output current, which aligns with the expected behavior in a boost converter. Higher output currents result in increased current flowing through the inductor, leading to higher core and copper losses. Additionally, the influence of input voltage is evident, with lower losses observed at higher input voltages for a given output current. This is consistent with the reduced current levels at higher input voltages due to the inverse relation among K and V_i in a boost converter. Further, the power loss analysis has been carried out at varying load conditions specifically 2.4 ohms to 24 ohms under different fixed input voltage conditions (V_i = 8 V, 12 V, and 16V) at 100 kHz frequency as shown in Fig. 9(b). At V_i = 8 V, the power loss depict the continuous reduction in trend ranging from 1.8 W at 2.4 ohms to 0.18 W at 24 ohms. Further, at V_i = 12 V, the power losses again represent the decrement from 1.20 W at 2.4 ohms to 0.12 W at 24 ohms. Similarly, at V_i = 16 V, the power losses again showcase a consistent decrement from 0.90 W at 2.4 ohms to 0.09 W at 24 ohms.

From the analysis, it is evident that the power losses in the inductor show a continuous trend. As the load resistance increases, the power losses in the inductor decrease, indicating a more efficient performance with higher load resistances. This behavior is expected as higher load resistances result in reduced current levels, leading to lower resistive losses in the inductor. Further, the impact of input voltage (V_i) on inductor power losses is apparent. At a fixed load resistance, the power losses decrease with increasing input voltage. This trend aligns with the inverse relation among K and V_i in a boost converter. As the duty cycle decreases with higher input voltage, the energy transfer efficiency improves, contributing to lower inductor power losses. Figure 11, shows the power loss investigations of the capacitor in a 12 V to 24 V boost converter at 100 kHz frequency. As shown in Fig. 11 (a) at an input voltage of 8V, capacitor losses increase gradually with higher output currents, ranging from 0.04 W at 1 A to 0.4 W at 10A Similarly, at 12V input, capacitor losses follow a similar pattern, increasing from 0.03 W to 0.30 W with rising output current. At 16 V input, these losses continue to exhibit an increase, varying from 0.02 W to 0.20 W.Particularly, for 12 V to 24 V boost converter, 0.06 W of capacitor power loss has been observed. From the results, it is evident that the



(a)



(b)

Fig. 11. Power loss analysis of capacitor at 100 kHz frequency at V_i= 8V, 12V, and 16V illustrating: (a) response related to I_o (b) response related to R_L

power losses in the capacitor depend upon load current. With the increment in load current, the power loss gradually increases. This behavior aligns with the conventional understanding of capacitor behavior in a boost converter, where increasing load currents lead to increased power losses in the capacitor due to factors such as increased ripple currents and higher stress on the capacitor components.

Further, the power loss analysis has been investigated at varying load conditions specifically 2.4 ohms to 24 ohms under different fixed input voltage conditions (8 V, 12 V, and 16V) at 100 kHz frequency as shown in Fig. 11(b). At V_i = 8 V, the power losses depict the continuous reduction ranging from 0.40 W at 2.4 ohms to 0.04 W at 24 ohms. Further, at V_i = 12 V, the power losses again depicts the decrement from 0.30 W at 2.4 ohms to 0.03 W at 24 ohms. Similarly, at V_i = 16 V, the power losses again showcase a consistent decrement from 0.20 W at 2.4 ohms to 0.02 W at 24 ohms. The decrease in capacitor power losses with increasing load resistance in a boost converter can be attributed to the impact of load resistance on the ripple current. In a boost converter, the capacitor experiences a pulsating current, known as the ripple

current, which is directly linked to the load resistance. As the load resistance increases, the ripple current ($\Delta I = V_o/8fR_LV_{cpp}$) tends to decrease.

Since the ripple current is a significant factor contributing to capacitor power losses a reduction in ripple current leads to lower power losses in the capacitor. Therefore, the decrease in load resistance results in lower ripple currents, subsequently reducing the power losses in the capacitor. This behavior aligns with the conventional understanding of capacitor behavior in boost converters, where higher load resistance tends to improve the capacitor's performance by minimizing ripple-related losses.

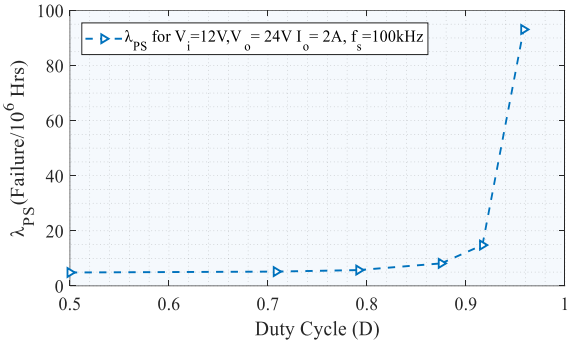
After analyzing the power losses of each power component, it becomes evident that predicting the accurate behavior and reliability just by observing the power losses in these components is challenging due to uncertainties in power losses. Therefore, to assess the actual behavior and reliability of the inductor, it is necessary to conduct a detailed evaluation and comparison of the separate failure rates of thes power components.

7.3. Evaluation of Reliability and Failure Rate

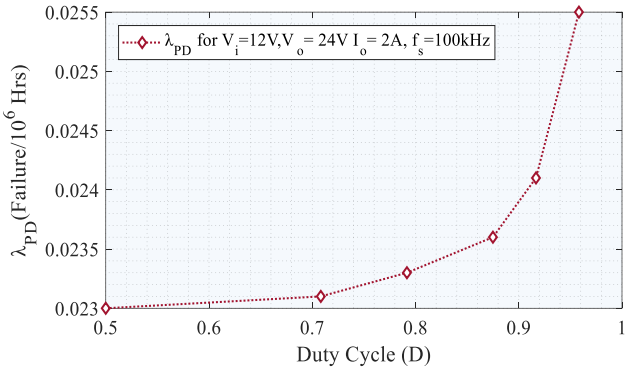
To analyze the behavior(including reliability) of the inductor, it is necessary to evaluate the separate failure rate and reliability of other power components like MOSFET, *D*, *L*, *C*, and *R*. The behavior and reliability of the inductor can be identified by comparing its failure rate and reliability. MIL-HDBK-217F handbook has been employed for analyzing the failure rate of individual components. Table 1 presents the expressions for failure rates (in *failure / 10^6 Hrs.)* and temperature factors of power components. Similarly, Table 2 shows the mathematical expressions for various thermal resistance, temperatures, and stress factors. In order to evaluate the part failure rate of the inductor (λ_{P_L}), the base failure rate has been selected (using the Military handbook) as 0.000030 *failure/10^6* Hrs. The temperature factor (π_T) has been obtained using the mathematical expression from Table 1 as 1.9144. Similarly the quality factor (π_Q) and environmental factors (π_E) have been selected as 3 & 6 respectively. Using Table 1 and Table 2, the failure rate of the *L* has been evaluated that is 0.001033776 *failure/10^6* Hrs.

In the same fashion, the failure rate of MOSFET (λ_{P_S}) has been calculated using Table 1 and Table 2. The base failure rate (λ_B) has been selected for 0.012 *failure/10^6* Hrs. Here is the temperature factor of MOSFET (π_T) has been evaluated as 1.5334. Similarly, the 'π_A ' 'π_Q ' and 'π_E ' have been selected as 8.0, 5.50, and 6.0 respectively. After evaluation of all necessary stress factors, the switch's failure rate has been obtained as 4.86 *failure/10^6* Hrs using Table 1. In a similar way, the failure rate of the diode (λ_{P_D}) has been evaluated as 0.0230 *failure/10^6* Hrs using Table 1. Here, the 'π_T ' has been obtained as 2.1510. Further, the 'π_Q ' 'π_s ', 'π_C ' and 'π_E ' have been evaluated as 5.5, 0.1078, 1, and 6 respectively. In the same manner, the failure rate has been evaluated for the capacitor (λ_{P_C}) and load (λ_{P_R}) through utilizing the mathematical equations from Table 1 and Table 2 as 0.0716843 and 1.7221 *failure/10^6* Hrs respectively.

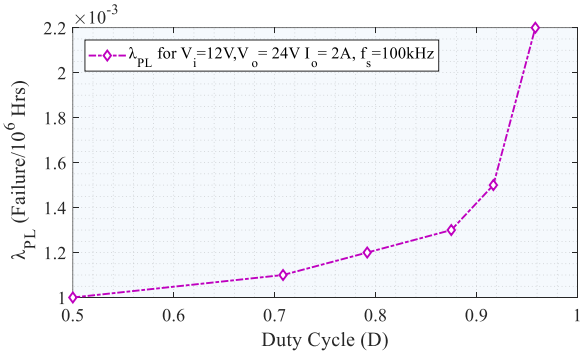
Figure 12 shows the reliability outcomes and analysis of failure rates of each component. Figure 12(a) to Figure 12(e), describe the failure rates of, the MOSFET, *D*, *L*, *C*, and *R* respectively. From the results, it is evident that the performance of the converter primarily relies on the careful



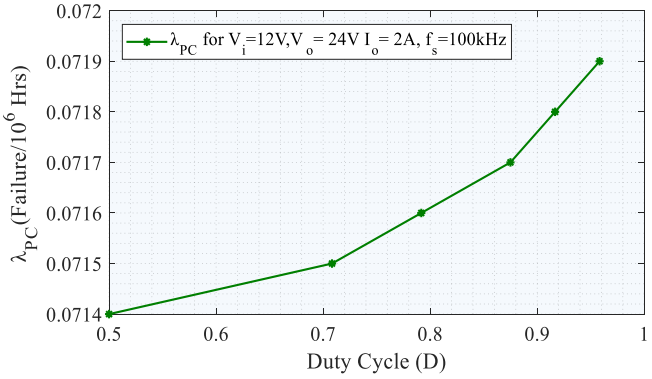
(a)



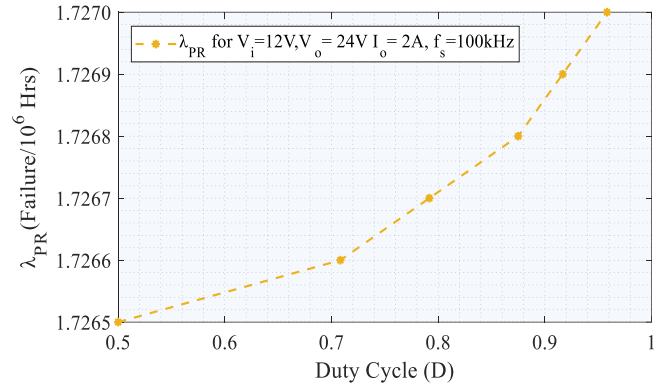
(b)



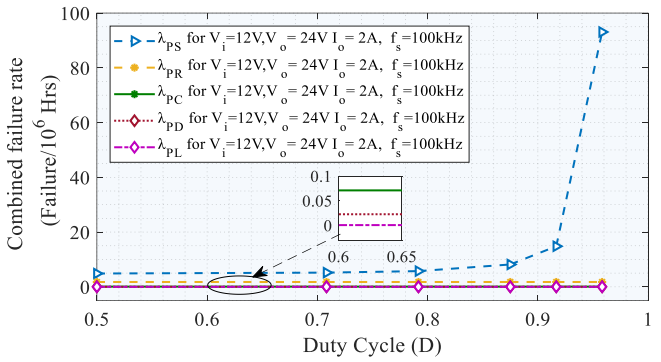
(c)



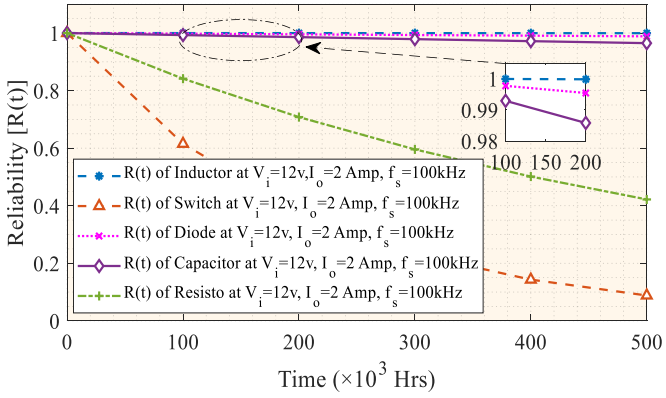
(d)



(e)



(f)



(g)

Fig. 12. Analysis of reliability & failure rate of power components in boost converter (a) failure rate behaviour 'switch (MOSFET) vs duty cycle' at f_s=100khz (b) failure rate response 'diode vs duty cycle' at f_s=100khz (c) failure rate response 'inductor vs duty cycle' at f_s=100khz (d) failure rate response 'capacitor vs duty cycle' at f_s=100khz (e) failure rate response 'resistor vs duty cycle' at f_s=100khz (f) combined 'failure rates vs duty cycle' of all power components at f_s=100khz (g) reliability comparison of all power components at f_s=100khz choice of *K*. The probability of failure increases at higher duty cycles. The assessment also indicates that the failure rate of the inductor is significantly lower compared to other components in a 12 V to 24 V boost converter. This confirms the minimal probability of failure, resulting in superior reliability and performance compared to other components. The results also showcase the highest failure rate of MOSFET. The failure rate comparison has been depicted in Fig. 12(f).

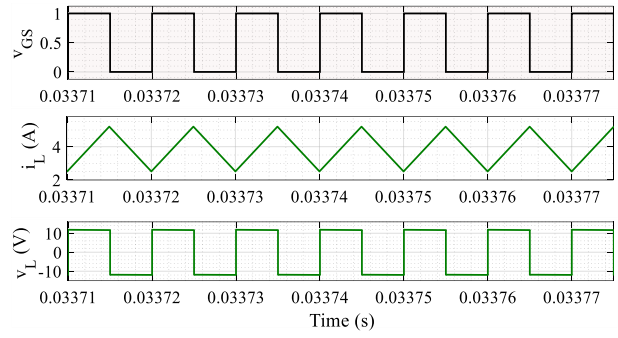
Finally, the reliability assessment and its comparison have been done through Eq. (18) for all circuit components as illustrated in Fig 12(g). According to the reliability assessment, the outcomes indicate lower reliability of the MOSFET switch, compared to other power elements that exhibit elevated failure rates. The results also showcase the highest reliability of the inductor, with a significantly lowerfailure rate compared to other circuit elements. This confirms its durability and sustained performance.

7.4. Current & Voltage Responses Across Inductor With Required V_o and I_o

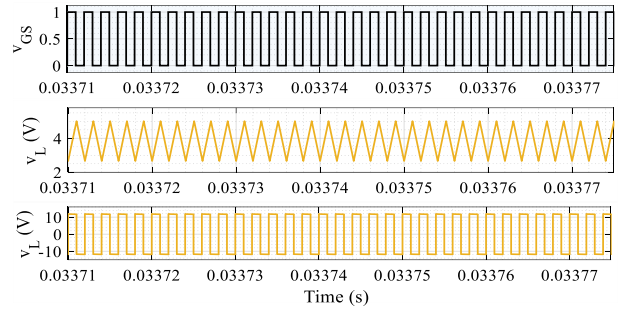
This work is primarily directed towards the design and assessment of the inductor's reliability. To perform this research, a 12V to 24V, 2 A transformerless DC-DC boost converter has been selected as a testing platform. Before analyzing the inductor design using the area product method and its reliability, the converter duty cycle has been obtained as 0.5 (or 50%). Further, the ripple current has been calculated as 8 A. The values of the inductor and capacitor have been evaluated as 7.5 µH and 83.33 µF respectively at 100 kHz and 1.5 µH and 16.66 µ*F* at 500 kHz.

Figures 13(a) & 13(b), depict the Matlab® Simulation outcomes of the current & voltage response across inductor '*L*' at 100 & 500 kHz frequencies. It is clear that the voltage and current across the inductor satisfy the converter requirements. In accordance with these requirements, the average inductor current should align with the DC input current of the converter. Simultaneously, the voltage across the inductor should be equivalent to the supply voltage. The results depicted in Fig. 13(a) & 13(b) clearly depict that the converter satisfies these conditions at both 100 and 500 kHz frequency. Further Fig. 13(c) and 13(d) showcase the results of the required load current (2 A) and voltage (24 V). In the presented case, with a 12V input and a desired 24V output at 2A, the boost converter adjusts the duty cycle to achieve the necessary voltage transformation. The boost converter operates by intermittently connecting and disconnecting the input voltage to an inductor. While the switch is in its on state, the inductor stores energy. This process causes a rise in the voltage across the inductor, helping to achieve the intended output voltage.

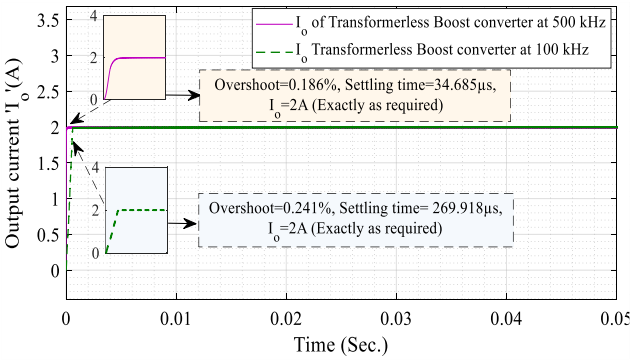
From the results [refer Fig. 13(c) & 13(d)] it is clear that the designed inductor supports the operation and plays a crucial role in providing a desired output voltage of 24V from a 12V input at 2Amp load current with very small overshoot (0.214% at 100 kHz 0.186% at 500 kHz) and settling time (269.918µs at 100 kHz and 34.685 µs at 500 kHz).



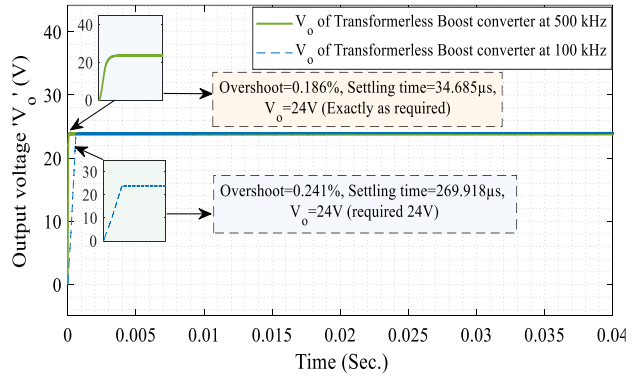
(a)



(b)



(c)



(d)

Fig. 13. Matlab® Simulation outcomes (a) current and voltage across the inductor at 100kHz (b) current and voltage across the inductor at 500kHz (c) Output current of boost converter at 100 & 500 kHz (Desired I_o =2 Amp) (d) Output voltage response of boost converter at 100 & 500 kHz (Desired V_o =24 V).

8. Conclusion

This paper offers comprehensive guidance for researchers on the design of magnetic components, specifically inductors, for 12V to 24V, 2A, 100kHz boost converter, commonly employed in various applications such as renewable energy systems and electric vehicles. The performance of a transformerless DC-DC boost converter is closely associated with the optimal design of the magnetic component, specifically the inductor. Several influencing elements, such as core type, core size, size of wire, and, turn count directly influence the inductor's reliability. A comprehensive assessment of such factors is crucial to ensure optimal reliability.

In this research work, the '*Area Product Methodology*' has been discussed regarding the evaluation of magnetic length (l_m), number of turns (N), cross-section area (A_{CS}), window area (W_A) of the core, the size of the wire (SWG), and the type of core shape. The findings clearly indicate that with an increase in output current, both A_p and W_A Increases. Furthermore, the analysis indicates that as output current (I_o) increases, both the number of turns (N) and the size of the wire decrease. Additionally, the study performed at 100 kHz & 500 kHz highlights that higher switching frequencies result in a reduction in the size of the inductor (L) and the number of turns (N). After following the proposed inductor design methodology for a 12V to 24V transformerless DC-DC boost converter at 2 A load current, an iron powder core (T44-26) has been selected at a frequency of 100 kHz that has an A_p of 0.0267 cm^4, requiring 18 rounds with a wire size of 19 SWG. Further, at a higher frequency (500 kHz), a T30-26 core has been selected that has an A_P of $0.0070 cm^4$, requiring 10 turn counts with 19 SWG size of wire.

This research work also showcases the performance of inductors concerning output current and load resistance. From the analysis, it is observed that an increase in output current results in a decrease in inductance. Further, the analysis has also been carried out under varying load conditions revealing that as the load changes, the inductance also experiences the change. The responses have also been scrutinized at a frequency of 500 kHz, indicating that at higher switching frequencies, the necessary inductance is lower, leading to a consequential reduction in core size. The reliability of power components is influenced by losses thus, a power loss assessment has been conducted for each power component, however, uncertainties have been identified in these losses. This analysis reveals that reliability cannot be justified or identified solely based on a single performance factor, such as power loss. To identify reliability, the evaluation of failure rates plays a crucial role. Therefore, the failure rate has been assessed for the inductor. Additionally, for performance comparison, the analysis has been carried out for other power components such as the diode, switch, capacitor, etc.

The results of the reliability evaluation include the failure rates for the inductor including other power components. The failure rate of the inductor at a 2A current is determined as 0.001033776 *failure/10^6* Hrs. Similarly, for the MOSFET, it is 4.86 *failure/10^6* Hrs, for the diode 0.0230 *failure/10^6*, and for the capacitor it is obtained as 0.0716843 *failure/10^6 Hours.* From the results, it is evident that the inductor has very high

reliability which is characterized by a lower failure rate. This confirms the inductor's durability and consistent performance in practical use. Additionally, the research work highlights the lower reliability of MOSFET, which demonstrates the highest failure rate among all the components.

This research contributes to the development of DC-DC converter technology and provides valuable knowledge for inductor design, behavior, and reliability, which will benefit the researchers and engineers working toward the design of power electronics converters for various applications.

References

[1] M. F. Akhtar, S. R. S. Raihan, N. A. Rahim, M. N. Akhtar, and E. A. Bakar, "Recent developments in DC-DC converter topologies for light electric vehicle charging: a critical review", Applied Sciences, vol. 13, no. 3, pp. 1676, 2023.

[2] F. A. Abbas, T. A. Abdul-Jabbar, A. A. Obed, A. Kersten, M. Kuder, and T. Weyh, "A Comprehensive Review and Analytical Comparison of Non-Isolated DC-DC Converters for Fuel Cell Applications", Energies, vol. 16, no. 8, pp. 3493, 2023.

[3] S. M. S. Hossain, M. A. Haque, R. Islam, and O. A. Mohammed, "A Review of Power Electronic Converters for Electric Aircrafts", in 2023 Fourth International Symposium on 3D Power Electronics Integration and Manufacturing (3D-PEIM), pp. 1-8, IEEE, 2023.

[4] K. Jayaswal and D. K. Palwalia, "Role of reliability assessment in Si-based non-Isolated DC-DC power electronic converters", Materials Today: Proceedings, vol. 60, pp. 1113-1119, 2022.

[5] B. W. Williams, "Basic DC-to-DC Converters", IEEE Transactions on Power Electronics, vol. 23, no. 1, pp. 387-401, 2008.

[6] K. Jayaswal and D. K. Palwalia, "Performance analysis of non-isolated DC-DC buck converter using resonant approach", Engineering, Technology & Applied Science Research, vol. 8, no. 5, pp. 3350-3354, 2018.

[7] Y. Guan, C. Cecati, J. M. Alonso, and Z. Zhang, "Review of high-frequency high-voltage-conversion-ratio DC–DC converters", IEEE Journal of Emerging and Selected Topics in Industrial Electronics, vol. 2, no. 4, pp. 374-389, 2021.

[8] S. Dahale, A. Das, N. M. Pindoriya, and S. Rajendran, "An overview of DC-DC converter topologies and controls in DC microgrid", in 2017 7th International Conference on Power Systems (ICPS), pp. 410-415, IEEE, 2017.

[9] K. Jayaswal, D. K. Palwalia, G. Jain, and P. Kumar, "Design-oriented analysis of non-isolated DC-DC buck converter", Ciencia e Tecnica Vitivinicola, vol. 30, pp. 177-213, 2015.

[10] A. M. S. Spencer Andrade, T. M. K. Faistel, R. A. Guisso, and A. Toebe, "Hybrid high voltage gain transformerless DC–DC converter", IEEE Transactions on Industrial Electronics, vol. 69, no. 3, pp. 2470-2479, 2021.

[11] X. L. Li, Z. Dong, K. T. C. Chi, and D. D.-C. Lu, "Single-inductor multi-input multi-output DC–DC converter with high flexibility and simple control", IEEE Transactions on Power Electronics, vol. 35, no. 12, pp. 13104-13114, 2020.

[12] G. Calderon-Lopez, J. Scoltock, Y. Wang, I. Laird, X. Yuan, and A. J. Forsyth, "Power-dense bi-directional DC–DC converters with high-performance inductors", IEEE Transactions on Vehicular Technology, vol. 68, no. 12, pp. 11439-11448, 2019.

[13] C. Cerda, F. Rojas, C. Pineda, J. Pereda, M. Diaz, J. Salgado, G. Droguett, D. Valdés, and G. Gatica, "Inductor design for a High-performance DC-DC Modular Multilevel Converter", 2019 IEEE CHILEAN Conference on Electrical, Electronics Engineering, Information and Communication Technologies (CHILECON), Valparaiso, Chile, pp. 1-7, 2019, doi: 10.1109/CHILECON47746.2019.8988111.

[14] C. W. M. T. Mclyman, Transformer and Inductor Design Handbook, CRC Press, 2016.

[15] D. Liang and H.-B. Shin, "Coupled inductor design method for 2-phase interleaved boost converters", Journal of Power Electronics, vol. 19, no. 2, pp. 344-352, 2019.

[16] X. Yu, J. Su, J. Lai, and S. Guo, "Analytical optimization of nonsaturated thermally limited high-frequency transformer/inductor design considering discreteness of design variables", IEEE Transactions on Power Electronics, vol. 35, no. 6, pp. 6231-6250, 2019.

[17] H. Radmanesh, M. R. Soltanpour, and M. E. Azizkandi, "Design and implementation of an ultra-high voltage DC-DC converter based on coupled inductor with continuous input current for clean energy applications", International Journal of Circuit Theory and Applications, vol. 49, no. 2, pp. 348-379, 2021.

[18] M. Mojibi and M. Radmehr, "Reliability evaluation of buck converter based on thermal analysis", Journal of Microelectronics, Electronic Components and Materials, vol. 48, pp. 217–227, 2018.

[19] M. H. Nguyen and S. Kwak, "Enhance reliability of semiconductor devices in power converters", Electronics, vol. 9, no. 12, pp. 2068, 2020.

[20] S. Rahimpour, H. Tarzamni, N. V. Kurdkandi, O. Husev, D. Vinnikov, and F. Tahami, "An Overview of Lifetime Management of Power Electronic Converters", IEEE Access, vol. 10, pp. 109688-109711, 2022, doi: 10.1109/ACCESS.2022.3214320.

[21] MIL-HDBK-217F, Military handbook: relibility prediction of electronic equipment, Department of defence, USA, 1995.

[22] K. Jayaswal, D. K. Palwalia, and S. Kumar, "Performance investigation of PID controller in

trajectory control of two-link robotic manipulator in medical robots", Journal of Interdisciplinary Mathematics, vol. 24, pp. 467-478, 2021.

[23] K. Jayaswal, D. K. Palwalia, and S. Kumar, "Analysis of robust control method for the flexible manipulator in reliable operation of medical robots during COVID-19 pandemic", Microsystem Technologies, vol. 27, no. 5, pp. 2103-2116, 2021.

[24] K. Jayaswal, D. K. Palwalia and J. M. Guerrero, "Design and Reliability Assessment of Inductor for Non-isolated DC-DC Buck Converter", 2023 First International Conference on Advances in Electrical, Electronics and Computational Intelligence (ICAEECI), Tiruchengode, India, 2023, pp. 1-8, doi: 10.1109/ICAEECI58247.2023.10370977.

[25] L. Militã, B. Bertoldi, A. G. L. Furlan, M. L. Heldwein and J. Riso Barbosa, "Thermal Network Models for Toroidal and E-Core Inductors in Still Air", IEEE Transactions on Power Electronics, vol. 38, no. 12, pp. 15872-15890, 2023.

[26] A. H. Ismail, Z. Ma, A. Al-Hmoud and Y. Zhao, "A High Frequency Coupled Inductor Design for High Power Density DC-DC Converters", IEEE Applied Power Electronics Conference and Exposition (APEC), Orlando, FL, USA, 2023, pp. 3275-3280, doi: 10.1109/APEC43580.2023.10131629.

[27] T. Manthey, M. Khader and J. Friebe, "Transformer Design Optimization and Comparison for a DC-DC Converter used in PV Micro-Inverters", 24th European Conference on Power Electronics and Applications (EPE'22 ECCE Europe), Hanover, Germany, 2022, pp. 01-06.

[28] S. M. Akbar, A. Hasan, A. J. Watson and P. Wheeler, "FEA Based Transformer Loss Analysis for Dual Active Bridge DC–DC Converter Using Triple Phase Shift Modulation", in IEEE Journal of Emerging and Selected Topics in Power Electronics, vol. 10, no. 4, pp. 4342-4355, Aug. 2022, doi: 10.1109/JESTPE.2022.2148355.

[29] H. Taghavi, A. El Shafei, and A. Nasiri, "Liquid Cooling System for a High Power, Medium Frequency, and Medium Voltage Isolated Power Converter", 2023 12th International Conference on Renewable Energy Research and Applications (ICRERA), pp. 405-413, IEEE, 2023.

[30] A. Sahbani, K. Cherif, and K. Ben Saad, "Multiphase Interleaved Bidirectional DC-DC Converter for Electric Vehicles and Smart Grid Applications", International Journal of Smart Grid-ijSmartGrid, vol. 4, no. 2, pp. 80-87, 2020.

[31] S. F. Jaber and A. M. Shakir, "Design and simulation of a boost-microinverter for optimized photovoltaic system performance", Int. J. SMART GRID (ijSmartGrid), vol. 5, no. 2, pp. 94-102, 2021.

[32] K. Kajiwara, R. Daimon, Y. Ohta, A. Segami, N. Matsui, and F. Kurokawa, "Voltage Balance of Multiconnected Half Bridge Converter", 2021 10th International Conference on Renewable Energy Research and Application (ICRERA), Istanbul, Turkey, 2021, pp. 439-442.

[33] K. Ikeda, Y. Iwasaki, A. Tanaka, T. Nishitani, K. Yukita, T. Nanahara, Y. Goto, and A. Kato, "Basic Characteristics of Converters with Special Winding Structure Transformers", 2022 11th International Conference on Renewable Energy Research and Application (ICRERA), pp. 293-298, IEEE, 2022.

[34] M. Vafadar, H. Vafadar, and A. Nasiri, "A DC-DC Converter with Multistage Boost Input and High Voltage Gain for Solar PV Applications", 2023 12th International Conference on Renewable Energy Research and Applications (ICRERA), pp. 52-58, IEEE, 2023.